Research Article

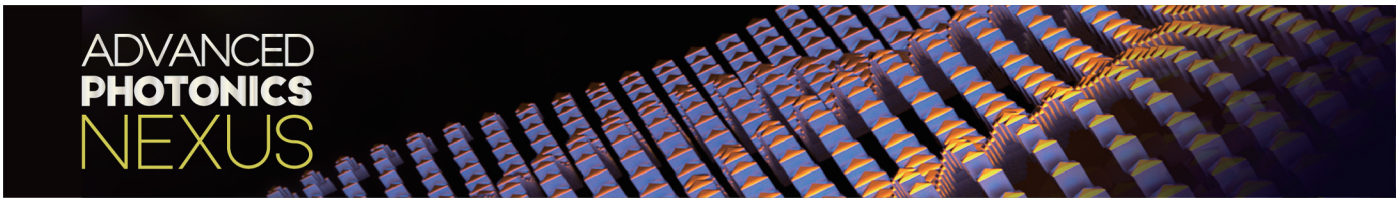

Optical reflective metasurfaces based on mirror-coupled slot antennas

Sven Ebel,[a,b] Yadong Deng,[a] Mario Hentschel,[c] Chao Meng,[a] Sören im Sande,[a] Harald Giessen,[c] Fei Ding,[a,*] and Sergey I. Bozhevolnyi[a,*]

[a]University of Southern Denmark, Center for Nano Optics, Odense, Denmark
[b]Kiel University, Institute for Experimental and Applied Physics, Kiel, Germany
[c]University of Stuttgart, Research Center SCoPE, 4th Physics Institute, Stuttgart, Germany

Abstract. Electrically connected optical metasurfaces with high efficiencies are crucial for developing spatiotemporal metadevices with ultrahigh spatial and ultrafast temporal resolutions. While efficient metal–insulator–metal (MIM) metasurfaces containing discretized meta-atoms require additional electrodes, Babinet-inspired slot-antenna-based plasmonic metasurfaces suffer from low efficiencies and limited phase coverage for copolarized optical fields. Capitalizing on the concepts of conventional MIM and slot-antenna metasurfaces, we design and experimentally demonstrate a new type of optical reflective metasurfaces consisting of mirror-coupled slot antennas (MCSAs). By tuning the dimensions of rectangular-shaped nanoapertures atop a dielectric-coated gold mirror, we achieve efficient phase modulation within a sufficiently large range of 320 deg and realize functional phase-gradient metadevices for beam steering and beam splitting in the near-infrared range. The fabricated samples show ($22\% \pm 2\%$) diffraction efficiency for beam steering and ($17\% \pm 1\%$) for beam splitting at the wavelength of 790 nm. The considered MCSA configuration, dispensing with auxiliary electrodes, offers an alternative and promising platform for electrically controlled reflective spatiotemporal metasurfaces.

Keywords: optical reflective metasurfaces; beam steering; beam splitting.

Received Sep. 29, 2022; revised manuscript received Nov. 24, 2022; accepted for publication Nov. 30, 2022; published online Jan. 2, 2023.

[DOI: 10.1117/1.APN.2.1.016005]

1 Introduction

In the past decade, optical metasurfaces have attracted considerable attention due to their superior capabilities of arbitrarily molding light, thereby challenging conventional bulky optics with ultrathin planar metadevices exhibiting compact footprints and advanced functionalities.[1–7] Typically, optical metasurfaces are made up of different types of fundamental building blocks called meta-atoms, such as single-layered metallic antennas,[8,9] slot antennas,[10–15] metal–insulator–metal (MIM) resonators,[16–20] and all-dielectric antennas,[21–24] which enable local control over the amplitude, phase, and polarization of optical fields by tailoring the meta-atom geometry and orientation. In terms of the efficiency, MIM meta-atoms, which are composed of a thin dielectric spacer sandwiched between an optically thick metal film and metallic antennas, are found to be superior to other counterparts regarding control of reflected optical fields, a circumstance that has resulted in their numerous technical applications.[6,16] In particular, electrically driven spatiotemporal MIM metasurfaces with dynamic optical responses have been successfully demonstrated by triggering the active media with applied voltages.[7,25–28] However, due to the discrete nature of metallic antennas, additional electrodes are necessarily required for their control, which not only complicates the design and fabrication but also affects the performance, hence restricting severely the applications for adaptive photonic systems.

Capitalizing on the concepts of conventional MIM metasurfaces and Babinet-inspired slot-antenna-based metasurfaces,[10–12] we design and experimentally demonstrate a new type of optical reflective metasurfaces composed of mirror-coupled slot antennas (MCSAs). By tuning the dimensions of subwavelength-

*Address all correspondence to Fei Ding, feid@mci.sdu.dk; Sergey I. Bozhevolnyi, seib@mci.sdu.dk

thick rectangular-shaped nanoapertures atop a dielectric silicon dioxide (SiO_2) coated gold (Au) mirror, we achieve a phase coverage up to 320 deg for linearly polarized excitation and realize functional phase-gradient metadevices for beam steering and beam splitting in the near-infrared range. The fabricated metasurfaces exhibit ($22\% \pm 2\%$) diffraction efficiency for beam steering and ($17\% \pm 1\%$) for beam splitting at the wavelength of 790 nm. The considered MCSA configuration offers an alternative and promising platform for optical reflective metasurfaces, especially for electro-optically tunable metasurfaces,[25–29] by virtue of using electrically connected meta-atoms and thereby dispensing with auxiliary electrodes.

2 Results and Discussion

2.1 Design of the Meta-atom

The designed MCSA unit cell consists of a rectangular-shaped slot antenna milled in a subwavelength-thick Au film, a middle SiO_2 spacer layer, and an optically thick Au mirror, forming a modified MIM meta-atom [Fig. 1(a)]. The periodicity of MCSA unit cells is $\Lambda = 240$ nm, which is much smaller than the design wavelength of $\lambda = 785$ nm to eliminate any free propagating diffraction orders. The thickness of the topmost slot antenna is $t_m = 50$ nm, and the thickness of the bottom Au layer is $t_{\text{sub}} = 100$ nm, which is thick enough to block the transmission. To study the optical response of the MCSA unit cell, we performed full-wave simulations with the commercially available finite-element software COMSOL Multiphysics (version 5.6). In simulations, the refractive index of the SiO_2 spacer layer is assumed to be 1.45, whereas the relative permittivity of Au is described by the Drude model fitted with the Johnson and Christy data,[30] with the plasma frequency being $\omega_p = 1.37 \times 10^{16}$ s^{-1} and the damping frequency being $\omega_d = 1.224 \times 10^{14}$ s^{-1}. The medium above and within slot antennas is chosen to be air with the refractive index of 1. The simulation domain of the unit cell is truncated at the air side with a perfectly matched layer to minimize the reflection. With this model, we calculated the complex reflection coefficients on the top of the slot antenna as a function of L_x and L_y for normally incident transverse magnetic (TM) polarized excitation (the electric field is polarized along the x axis) at $\lambda = 785$ nm.

It is seen [Fig. 1(b)] that the variation of both L_x and L_y results in the phase variation for the reflected TM-polarized light in a wide range (up to 320 deg) at a relatively large spacer thickness $t_s = 130$ nm. This variation occurs because of tuning the meta-atom in the vicinity of the mode resonance formed by hybridization between the lateral plasmonic resonance confined in the slot antenna and vertical Fabry–Pérot (FP) resonance between the slot antenna and the bottom Au mirror. In contrast to the well-studied freestanding slot antenna that exhibits limited phase coverage of only 180 deg for the copolarized electric fields, the bottom Au film functions as a reflecting mirror of the FP cavity (Fig. S1 in the Supplementary Material). Therefore, the incident light will bounce back and forth before being reflected with a sufficiently large phase shift. Close to the plasmonic resonance that is indicated by the pronounced absorption of the TM-polarized incident light, the phase varies strongly, with a range of ~180 deg [Fig. 1(b)]. Away from the resonance region, the reflection phase is gradually varied with the lateral dimensions. For example, the reflection contribution of the top slot-antenna layer will be dominating when the slot antennas are narrow in the polarization direction, leading to the incident wave being mostly reflected by the top slot-antenna layer that approximates a continuous Au film [Figs. 1(b) and 1(c) and Figs. 2(a) and 2(c)]. When the slot antennas are wide, the top Au layer becomes more transparent, and the light is mainly reflected by the bottom Au layer. Therefore, the reflection phase changes with the thickness of the middle spacer [Fig. 1(b) and Figs. 2(a) and 2(b)]. According to the theory of Babinet-inspired plasmonic metasurfaces,[10–12] the phase shift φ_{xx} under TM-polarized excitation should be mainly determined by the length of the slot antenna along the y direction. However, the phase contours of such an MCSA unit cell are not parallel to each other, since the slot dimension along the x axis changes the accumulated charges and finally affects the resonance, especially in the strong absorption regime. The cross sections of the x component of the electric field (color map) and the electric field vectors (arrows) for different cutting planes through the center of the topmost slot antenna, where the electric field is strongly localized within the slot area [Fig. 1(c)], reveal the localized character of the slot mode. The maximal field strengths are found at the edges perpendicular to the polarization direction of the excitation. This observation is consistent with the studies on the transmission of light through differently shaped holes, where the resonant optical transmission is accompanied by an increased local field within the nanoholes.[31–33]

Owing to the hybrid plasmonic/FP resonance, the phase modulation for the reflected polarized light thereby depends heavily on the SiO_2 spacer thickness t_s, which influences the accessible phase coverage together with the absorption around the resonance of the slot antenna. Figure 2 depicts the phase dependence on the slot dimensions for two different spacer thicknesses. For a thickness of $t_s = 50$ nm, the phase space of around 320 deg is still accessible [Fig. 2(a)]. In contrast to the case with a thicker spacer of 130 nm, we observe a steeper phase variation in the region of resonance. Specifically, the phase contours become crammed close to each other for a smaller spacer thickness, different from Fig. 1(b). Meanwhile, the absorption becomes stronger with a more pronounced and narrower resonance. Therefore, this thickness is not ideal for a practicable accurate selection of slot-antenna candidates, even though similar phase contours can be found in other regions away from the resonance. The field distribution of the x-component of the electrical field is still strongly localized within the hole volume, as shown in Fig. 2(c). In comparison to the field localization at a 130-nm spacer thickness in Fig. 1(c), a decrease in field strength is observable. Further decreasing the spacer thickness to 10 nm causes a change in the phase distribution and reflectivity as well as in the field localization [Figs. 2(b) and 2(d)]. The resulting phase space is confined to a limited interval of only ~50 deg [Fig. 2(b)]. Additionally, the resonant structure does not show a strong localization, where the x component of the electrical field is only confined at the edges of the slot antenna for this 10-nm-SiO_2 configuration [Fig. 2(d)]. As a result, we choose a 130-nm spacer thickness for the following numerical and experimental discussions, since it provides a sufficiently large phase coverage with more spreading phase contours and higher reflection amplitudes.

2.2 Functional Phase-Gradient MCSA Metasurfaces for Beam Steering

To demonstrate the applicability of this kind of MCSA meta-atom, we design a phase-gradient metasurface that functions

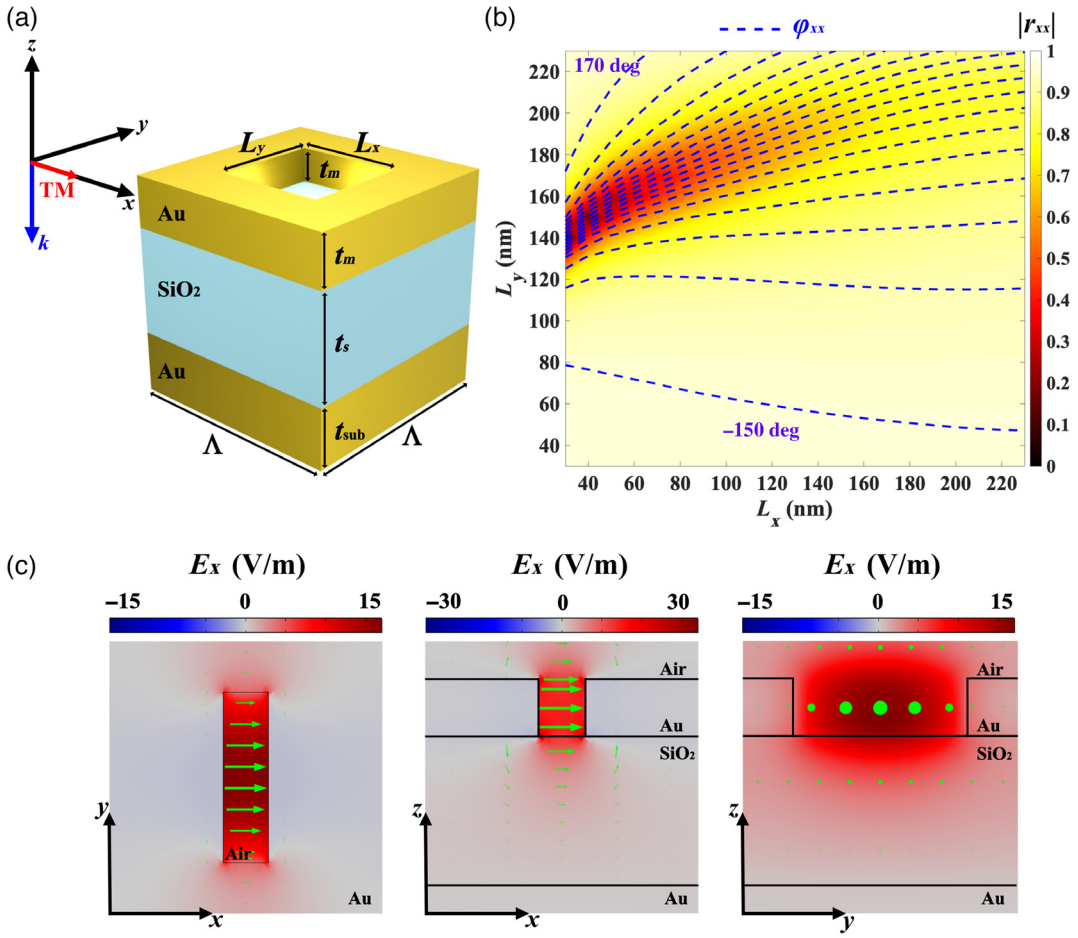

Fig. 1 (a) Schematic of the basic MCSA unit cell consisting of a slot antenna on top of an SiO_2 spacer and an Au mirror. (b) Numerically calculated complex reflection coefficients as a function of the slot antenna lateral dimensions at the design wavelength of $\lambda = 785$ nm upon TM polarization. The SiO_2 spacer thickness is set to $t_s = 130$ nm. The amplitude $|r_{xx}|$ is visualized by the color map, while the dashed blue lines are the contours of the reflection phase φ_{xx} ascending by a 20-deg phase step. (c) Cross-sectional electric field distributions in different cutting planes for the slot antenna with $L_x = 40$ nm and $L_y = 150$ nm at $\lambda = 785$ nm. The selected cutting planes display the mode profiles within the center of the slot antenna in the top Au layer. The color bars are chosen for illustrating the mode amplitude profiles of the E_x-component, while arrows indicate the electric field vectors at a representative moment of time.

as a beam steerer. Under the excitation of a TM-polarized wave at normal incidence, the reflected light will be redirected to a specific direction, which is well described by the generalized Snell's law[8] and may be also viewed as a blazed grating where the angle of reflection reassembles the first-order diffraction.[34] By marking the reflection phase through constant phase-contour lines in the complex reflection coefficient map, we select three meta-atoms with a nearly constant phase shift between neighbors and considerably high reflectivities according to realistic fabrication sizes. (The selected dimensions are shown in Table S1 and Fig. S2 in the Supplementary Material) Specifically, the chosen MCSA meta-atoms have a constant phase interval of ~110 deg between each other. The selected meta-atoms are then placed at a center-to-center distance of $\Lambda = 240$ nm to form a supercell. However, the supercell design is nontrivial, since two important factors should be considered. First, the supercell period should be larger than the incident wavelength to avoid coupling to surface plasmons.[35–37] Therefore, each meta-atom should be duplicated to make a bigger supercell, resulting in a decreased diffraction angle. Second, the arrangement of slot antennas within the supercell leads to the intrinsic near-field coupling between differently sized elements since the gradient-wise slot-antennas assembly is different from the array-wise arrangement with the identical unit cells during the design of the MCSA unit cell. Compared to conventional MIM metasurfaces composed of isolated metallic antennas that exhibit weak near-field coupling effects,[38] this MCSA metasurface is strongly affected by the near-field coupling. Since all meta-atoms are naturally connected, the charges induced by the electric fields are not confined anymore, thereby strongly modifying the responses of neighboring size-different elements (Fig. 3). The effect of this near-field coupling on the metasurface performance was studied numerically by considering three different supercells made of double, triple, and quadruple identical

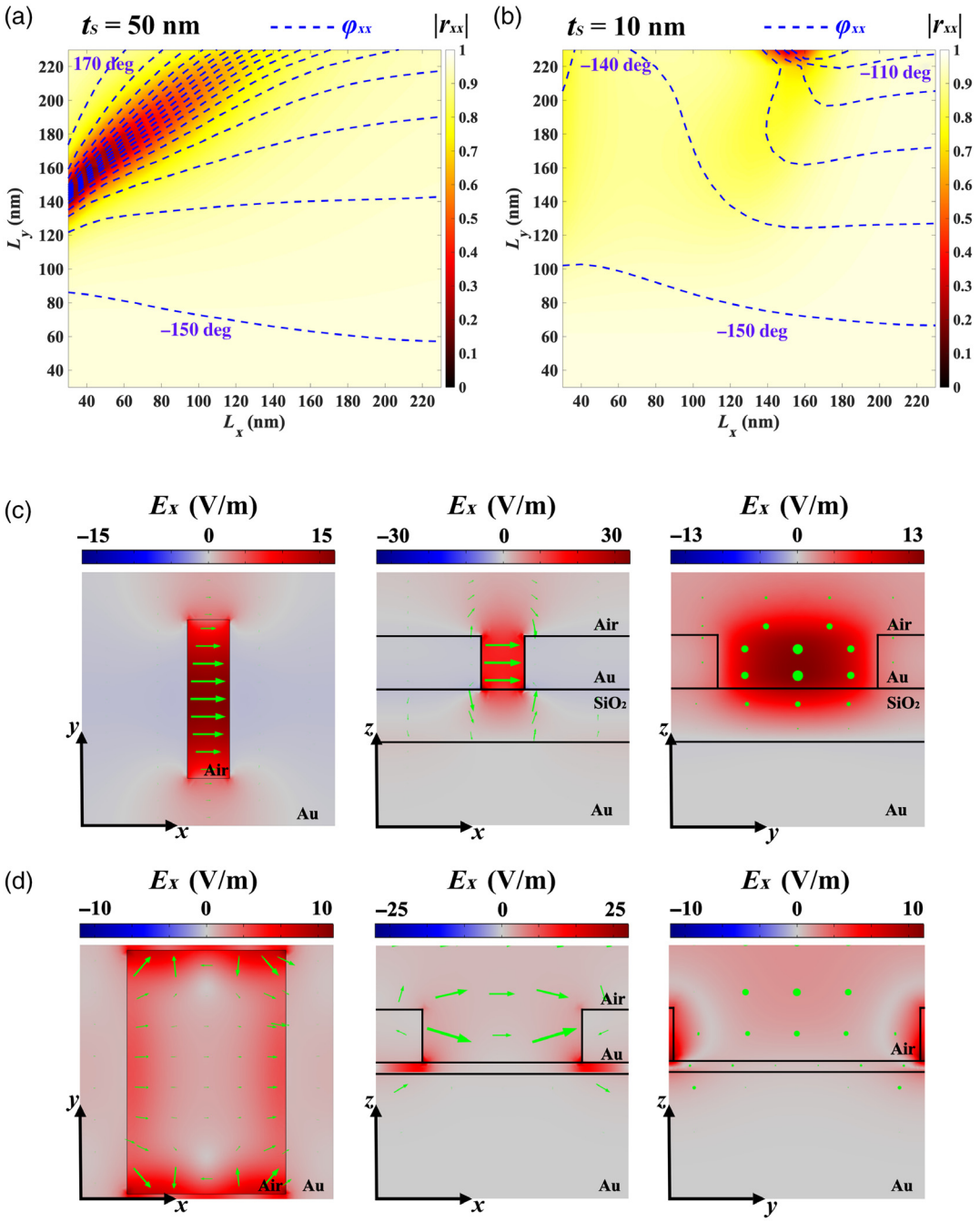

Fig. 2 (a), (b) Numerically calculated complex reflection coefficients as a function of the slot antenna's lateral dimensions at the design wavelength of $\lambda = 785$ nm upon TM polarization. The amplitude $|r_{xx}|$ is visualized by the color map, while the dashed blue lines are the contours of the reflection phase φ_{xx} ascending by (a) a 20-deg phase step and (b) a 10-deg phase step. The SiO_2 spacer thickness is set to $t_s = 50$ nm in (a) and $t_s = 10$ nm in (b). (c), (d) Cross-sectional electric field distributions in different cutting planes for the slot antenna at $\lambda = 785$ nm. The selected cutting planes display the mode profiles within the center of the slot antenna in the top Au layer. The color bars are chosen for illustrating the mode amplitude profiles of the E_x-component, while arrows indicate the electric field vectors at a representative moment of time. (c) The SiO_2 spacer thickness is set to $t_s = 50$ nm and the slot-antenna dimensions are $L_x = 40$ nm and $L_y = 150$ nm. (d) The SiO_2 spacer thickness is set to $t_s = 10$ nm and the slot-antenna dimensions are $L_x = 150$ nm and $L_y = 230$ nm.

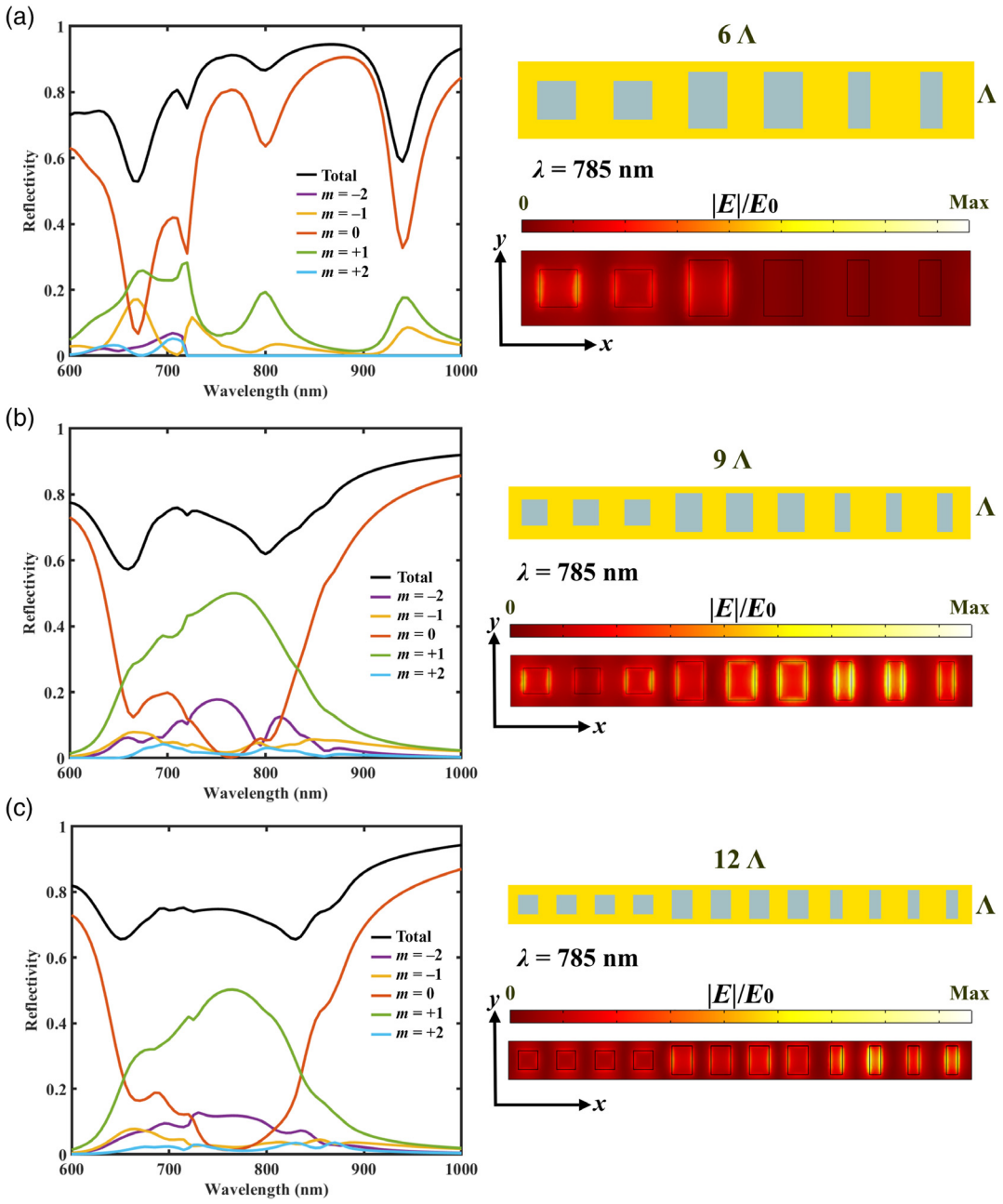

Fig. 3 Theoretical performance of the beam-steering MCSA metasurfaces that reflect the normal incident TM-polarized light into the +1 diffraction order for supercells consisting of (a) pair, (b) triple, and (c) quadruple identical MCSA meta-atoms. The left columns display the simulated diffraction efficiencies of different orders as a function of wavelength. The right columns show the electrical field distributions at the x–y plane cut from the center of the top slot-antenna layer at the wavelength of $\lambda = 785$ nm.

meta-atoms, leading, respectively, to the periods of 6Λ, 9Λ, and 12Λ along the x axis and the diffraction angles θ_r of 33 deg, 21.3 deg, and 15.8 deg at the wavelength of $\lambda = 785$ nm, respectively, as dictated by the first-order diffraction compatible also with the generalized Snell's law: $\theta_r = \sin^{-1}\frac{\lambda}{N\Lambda}$,[8] where N is the number of supercell elements. For the numerical studies of all metasurfaces, periodic boundary conditions are applied to the vertical sides and x polarized plane waves are impinging on the metasurfaces at normal incidence along the negative z axis. The diffraction efficiencies are obtained by normalizing the reflection into different diffraction orders.

As shown in Figs. 3(b) and 3(c), the supercells consisting of 9 and 12 elements perform well for steering the incoming light to the first diffraction order (green solid line), each reaching a diffraction efficiency of ~50% at $\lambda = 785$ nm. Still, the performance of the 12-element supercell can be considered more advantageous, since the reflectivity into the unwanted diffraction orders, mainly the −2 diffraction order (violet solid line), is

more suppressed compared to the 9-element design. For the six-element design [Fig. 3(a)], the specular reflection is dominating while the desired diffraction order is relatively low, which can be explained by plotting the electric field distributions within the top $x-y$ plane cut at the center of the slot antenna (right column in Fig. 3). It is clearly observable that the fields within the identical meta-atoms become more similar when the tuple size of the supercell is increased. As a final comment, it should be mentioned that the influence of near-field coupling between neighboring meta-atoms with significantly varied dimensions could also be decreased by inserting more meta-atoms with intermediate reflection phases (instead of the meta-atom multiplication considered above) to provide a smoother phase gradient and better performance (Fig. S3 in the Supplementary Material). However, this design is rather challenging to faithfully reproduce during the fabrication, since the neighbor slot dimensions are too close.

2.3 Experimental Demonstration of Functional MCSA Metasurfaces

Following the design, we fabricated the beam-steering MCSA metasurface composed of 12-element supercells on a silicon substrate using thin-film deposition, electron beam lithography, lift-off, and ion-beam etching techniques. First, a 2-nm chromium (Cr) adhesion layer and a 130-nm Au layer are evaporated on a silicon substrate using electron beam evaporation. Subsequently, a 140-nm-thick spin-on dielectric is applied (IC1-200, Futurrex, nominal refractive index of 1.34, hard-baked at 200 deg), which serves as the dielectric spacer layer with an equal optical thickness to the original design. Next, a 2-nm Cr adhesion and a 50-nm Au layer are deposited using electron beam evaporation. We use electron beam lithography (Raith Voyager, 50 kV acceleration voltage, beam current 2.14 nA) to define the structures in a positive tone resist (AR-P 6200.13, Allresist, area dose 160 $\mu C/cm^2$). After development, the resist mask is transferred to the underlying Au layer by Ar ion-beam etching (Technics Plasma). The remaining resist layer is removed in NEP at 80 °C (N-Ethyl-2-pyrrolidone). The fabricated metasurface has a size of 100 $\mu m \times 100$ μm, whose scanning electron microscopy (SEM) images are displayed in Fig. 4(b). Generally, the fabricated slot antennas resemble very well the desired shapes and dimensions, despite the inevitable surface roughness and rounded corners. The measurements were performed using a custom-built optical setup (Fig. S4 in the Supplementary Material) within the wavelength interval of 700 to 850 nm in steps of 10 nm. The inset optical image of the diffraction spots in Fig. 4(c) illustrates the beam-steering ability of the fabricated metasurface at the wavelength of $\lambda = 790$ nm, nearest to the design wavelength. To determine the overall performance quantitatively, we measured the corresponding diffraction efficiencies of different orders from $m = -2$ to +2. In the measurement, four fabricated metasurfaces with identical recipes were measured independently to calculate the mean value and corresponding standard errors of the mean. From Fig. 4(c), it is evident that the total reflectivity is close to 40%, and the diffraction efficiency of the +1 order is $(22\% \pm 2\%)$ at $\lambda = 790$ nm. Further, results show that beam-steering capability is pursued in a broadband spectrum ranging from 700 to 800 nm with zeroth order below 10% and higher diffraction orders suppressed below 5%. Compared to the averaged reflectance of the three selected MCSA meta-atoms

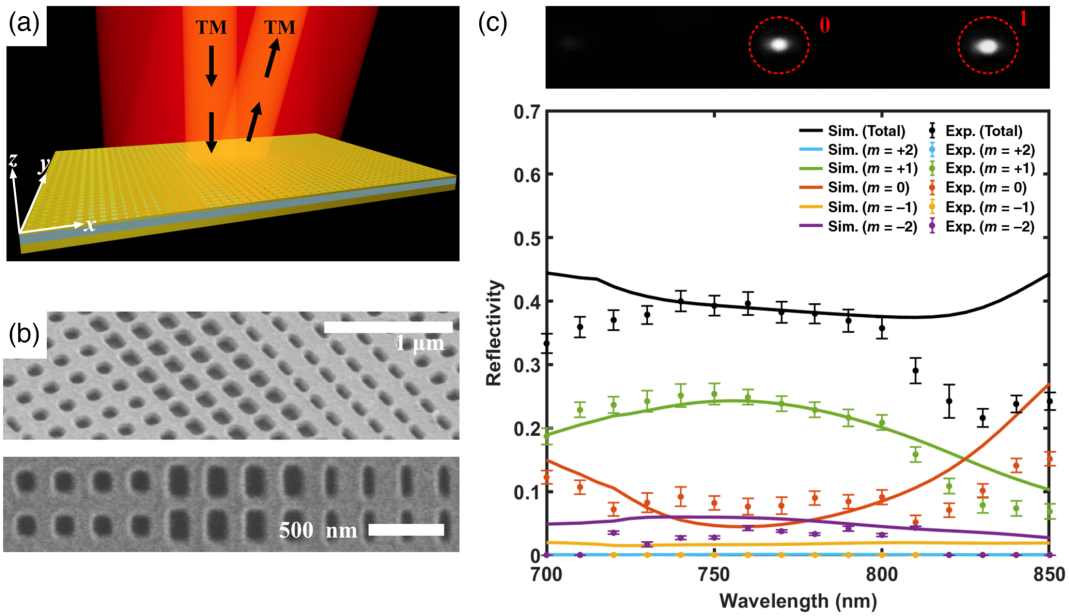

Fig. 4 (a) Schematic illustration of the MCSA reflective metasurface for beam steering. (b) SEM images of the fabricated beam-steering metasurface. The lower image depicts the fabricated supercells. (c) Simulated (solid lines) and experimental (dots with error bars) diffraction efficiencies of different orders as a function of wavelength for TM incident light. The error bars denote the standard deviation of the measured data of four metasurface samples. The inset image shows the diffracted light spots at $\lambda = 790$ nm, whose intensity has been adjusted for the visualization.

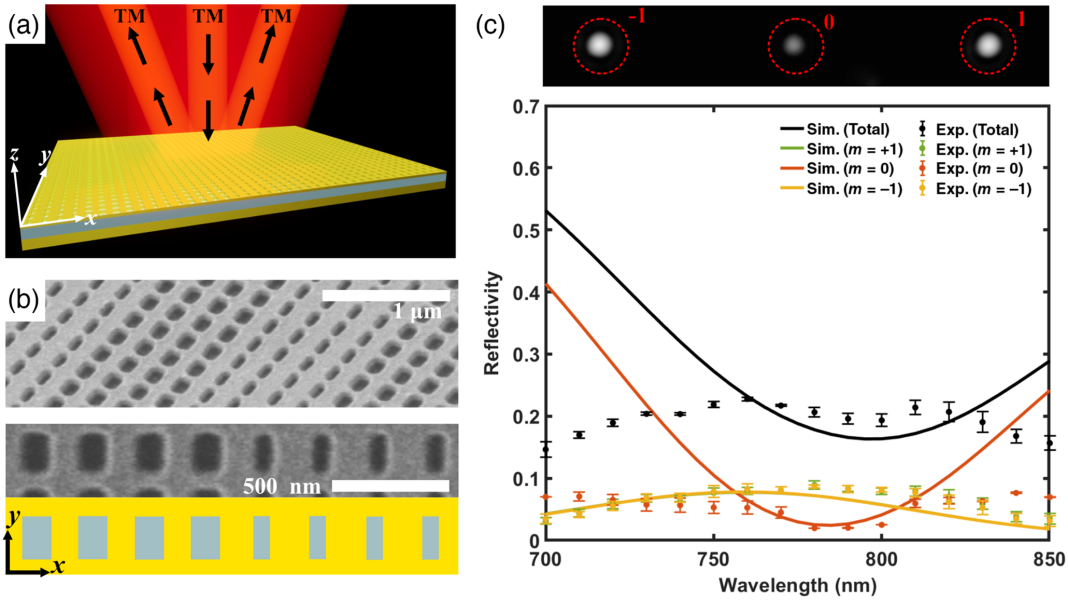

Fig. 5 (a) Schematic illustration of the MCSA reflective metasurface for beam splitting. (b) SEM images of the fabricated beam-splitting metasurface. The lower image shows the designed and fabricated supercells. (c) Simulated (solid lines) and experimental (dots with error bars) diffraction efficiencies of different orders as a function of wavelength for TM incident light. The error bars denote the standard deviation of the measured data of four metasurface samples. The inset image shows the diffracted light spots at $\lambda = 790$ nm, whose intensity has been adjusted for the visualization.

(~47%) at $\lambda = 790$ nm, the measured diffraction efficiency is reduced by half, which is mainly ascribed to the increased dissipation loss from the 2-nm-thick Cr adhesion layer as well as the surface scattering and grain boundary effects of the deposited Au layers. To validate our assumptions, we increased the damping rate of Au by a factor of 3 in the simulation and obtained reasonably matched simulation results with the measurements.

For further validation of the MCSA concept, an additional metasurface was designed and fabricated that enables splitting the incoming TM wave into ± 1 diffraction orders with equal intensity, which is made up of a quadruple arrangement of the two slot antennas with the phase difference of ~180 deg (Fig. 5). This leads to a supercell consisting of eight elements with a diffraction angle of $\theta_r = 24$ deg at the design wavelength of $\lambda = 785$ nm.[8] The SEM images of part of the fabricated sample are shown in Fig. 5(b). Similarly, the fabricated beam-splitting metasurface samples were characterized by measuring the diffraction efficiencies into different orders in Fig. 5(c). We again observe a reasonable agreement between the simulated and measured results in a wide wavelength range. At the measured wavelength of $\lambda = 790$ nm, $(17\% \pm 1\%)$ of the incident wave is split into the ± 1 diffraction orders, whereas the total reflectivity almost reaches ~20%. Due to increased ohmic losses in metallic layers (as compared to the tabulated values) especially at shorter wavelengths, the total reflectivity in the simulation and experiment exhibits different dependences on the optical wavelength. As a final comment, we emphasize that the efficiencies of MCSA metasurfaces could be further improved using single-crystalline metallic materials in the fabrication process to reduce the ohmic loss.[39,40]

3 Conclusion

We have demonstrated a new type of reflection optical metasurface based on MCSAs, which combine the advantages of high efficiencies and ease of fabrication from conventional MIM metasurfaces as well as the electrical connection from Babinet-inspired slot-antenna-based metasurfaces. By tuning the lateral dimensions of the slot antennas and optimizing the spacer thickness, a phase coverage of 320 deg can be achieved for the copolarized reflected light. With this platform, we have implemented functional phase-gradient metasurfaces that perform beam steering and beam splitting in the near-infrared wavelength range. Reasonably good working performance, in terms of efficiencies and operation bandwidths, was achieved by alleviating the near-field coupling between adjacent differently sized meta-atoms. We believe that this newly established reflective metasurface configuration with electrically connected individual elements offers an alternative and promising platform for electrically controlled reflective metasurfaces.

Acknowledgments

S. Ebel and Y. Deng contributed equally to this work. This work was funded by the Villum Fonden (Award in Technical and Natural Sciences 2019 and Grant No. 37372) and Danmarks Frie Forskningsfond (Grant No. 1134-00010B). C. Meng would like to acknowledge the support from the European Union's Horizon 2020 Research and Innovation Program under the Marie Skłodowska-Curie Action (Grant Agreement No. 713694). Y. Deng would like to acknowledge the support from the China Scholarship Council (Grant No. 202108330079). M. Hentschel and H. Giessen would like to acknowledge the

support from the Deutsche Forschungsgemeinschaft; Bundesministerium für Bildung und Forschung; ERC Advanced Grant (COMPLEXPLAS); Alexander von Humboldt Foundation and the Carl Zeiss Stiftung.

Code, Data and Materials Availability

The simulated and experimental data that support the works of this study are available from the corresponding authors on reasonable request.

References

1. A. V. Kildishev, A. Boltasseva, and V. M. Shalaev, "Planar photonics with metasurfaces," *Science* **339**, 1232009 (2013).
2. N. Yu and F. Capasso, "Flat optics with designer metasurfaces," *Nat. Mater.* **13**(2), 139–150 (2014).
3. H.-T. Chen, A. J. Taylor, and N. Yu, "A review of metasurfaces: physics and applications," *Rep. Progr. Phys.* **79**(7), 076401 (2016).
4. H. H. Hsiao, C. H. Chu, and D. P. Tsai, "Fundamentals and applications of metasurfaces," *Small Methods*, **1**(4), 1600064 (2017).
5. F. Ding, A. Pors, and S. I. Bozhevolnyi, "Gradient metasurfaces: a review of fundamentals and applications," *Rep. Prog. Phys.* **81**(2), 026401 (2018).
6. S. L. Sun et al., "Electromagnetic metasurfaces: physics and applications," *Adv. Opt. Photonics* **11**, 380–479 (2019).
7. A. M. Shaltout, V. M. Shalaev, and M. L. Brongersma, "Spatiotemporal light control with active metasurfaces," *Science* **364**, eaat3100 (2019).
8. N. Yu et al., "Light propagation with phase discontinuities: generalized laws of reflection and refraction," *Science* **334**, 333–337 (2011).
9. E. Karimi et al., "Generating optical orbital angular momentum at visible wavelengths using a plasmonic metasurface," *Light Sci. Appl.* **3**, e167 (2014).
10. F. Falcone et al., "Babinet principle applied to the design of metasurfaces and metamaterials," *Phys. Rev. Lett.* **93**, 197401 (2004).
11. T. Zentgraf et al, "Babinet's principle for optical frequency metamaterials and nanoantennas," *Phys. Rev. B* **76**, 033407 (2007).
12. X. Ni et al., "Ultra-thin, planar, Babinet-inverted plasmonic metalenses," *Light Sci. Appl.* **2**, e72 (2013).
13. S. Wang, D. C. Abeysinghe, and Q. Zhan, "Generation of vectorial optical fields with slot-antenna-based metasurface," *Opt. Lett.* **40**, 4711–4714 (2015).
14. M. Q. Mehmood et al., "Visible-frequency metasurface for structuring and spatially multiplexing optical vortices," *Adv. Mater.* **28**, 2533 (2016).
15. M. Habib et al., "Wavefront control with nanohole array-based out-of-plane metasurfaces," *ACS Appl. Nano Mater.* **4**(9), 8699 (2021).
16. S. Sun et al., "High-efficiency broadband anomalous reflection by gradient meta-surfaces," *Nano Lett.* **12**(12), 6223–6229 (2012).
17. A. Pors et al., "Gap plasmon-based metasurfaces for total control of reflected light," *Sci. Rep.* **3**, 2155 (2013).
18. F. Ding et al., "A review of gap-surface plasmon metasurfaces: fundamentals and applications," *Nanophotonics* **7**, 1129–1156 (2018).
19. Y. Deng et al., "Functional metasurface quarter-wave plates for simultaneous polarization conversion and beam steering," *ACS Nano.* **15**, 18532 (2021).
20. D. Lin et al., "Dielectric gradient metasurface optical elements," *Science* **345**, 298–302 (2014).
21. A. Arbari et al., "Dielectric metasurfaces for complete control of phase and polarization with subwavelength spatial resolution and high transmission," *Nat. Nanotechnol.* **10**, 937–943 (2015).
22. M. Khorasaninejad et al., "Arbitrary spin-to-orbital angular momentum conversion of light," *Science* **352**, 1190–1194 (2016).
23. A. Kuznetsov et al., "Optically resonant dielectric nanostructures," *Science* **354**, aag2472 (2016).
24. C. Zhang et al., "Low-loss metasurface optics down to the deep ultraviolet region," *Light Sci. Appl.* **9**(1), 55 (2020).
25. P. Thureja et al., "Array-level inverse design of beam steering active metasurfaces," *ACS Nano* **14**(11), 15042 (2020).
26. J. Park et al., "All-solid-state spatial light modulator with independent phase and amplitude control for three-dimensional LiDAR applications," *Nat. Nanotechnol.* **16**, 69–76 (2021).
27. C. Damgaard-Carstensen et al., "Electrical tuning of Fresnel lens in reflection," *ACS Photonics* **8**(6), 1576 (2021).
28. A. Weiss et al., "Tunable metasurface using thin-film lithium niobate in the telecom regime," *ACS Photonics* **9**(2), 605 (2022).
29. J. Karst et al., "Electrically switchable metallic polymer nanoantennas," *Science* **374**, 612–616 (2021).
30. P. B. Johnson and R. W. Christy, "Optical constants of the noble metals," *Phys. Rev. B* **6**, 4370 (1972).
31. T. W. Ebbesen et al., "Extraordinary optical transmission through sub-wavelength hole arrays," *Nature* **391**, 667–669 (1998).
32. F. J. García-Vidal et al., "Transmission of light through a single rectangular hole," *Phys. Rev. Lett.* **95**, 103901 (2005).
33. H. Guo et al., "Optical resonances of bowtie slot antennas and their geometry and material dependence," *Opt. Express* **16**, 7756–7766 (2008).
34. S. Larouche and D. R. Smith, "Reconciliation of generalized refraction with diffraction theory," *Opt. Lett.* **37**, 2391 (2012).
35. S. Sun et al., "Gradient-index meta-surfaces as a bridge linking propagating waves and surface waves," *Nat. Mater.* **11**, 426–431 (2012).
36. F. Ding, R. Deshpande, and S. I. Bozhevolnyi, "Bifunctional gap-plasmon metasurfaces for visible light: polarization-controlled unidirectional surface plasmon excitation and beam steering at normal incidence," *Light Sci. Appl.* **7**, 17178 (2018).
37. F. Ding and S. I. Bozhevolnyi, "A review of unidirectional surface plasmon polariton metacouplers," *IEEE J. Sel. Top. Quantum Electron.* **25**(3), 4600611 (2019).
38. R. Deshpande et al., "Direct characterization of near-field coupling in gap plasmon-based metasurfaces," *Nano Lett.* **18**, 6265–6270 (2018).
39. S. Boroviks et al., "Use of monocrystalline gold flakes for gap plasmon-based metasurfaces operating in the visible," *Opt. Mater. Express* **9**, 4209–4217 (2019).
40. S. Boroviks et al., "Extremely confined gap plasmon modes: when nonlocality matters," *Nat. Commun.* **13**, 3105 (2022).

Sven Ebel received his BS degree from Kiel University in 2020. He is currently a master student at the Institute for Experimental and Applied Physics, Kiel University, Germany. He holds one issued patent. His research interests include metasurfaces and electron–light interactions in ultrafast electron microscopy.

Yadong Deng received his bachelor's degree in electronic science and technology from Xuzhou University of Technology, China, in 2017 and his master's degree in physics from Zhejiang Normal University, China, in 2020. After 1-year research assistant at the Center for Nano Optics, University of Southern Denmark (SDU Nano Optics), Denmark, he is currently one full-time PhD student at SDU Nano Optics since 2021. His fields of interest include nanophotonics, plasmonics, and metasurfaces.

Mario Hentschel studied physics in Bonn, finishing his diploma thesis with Manfred Fiebig in 2009. He moved to the group of Harald Giessen (of Stuttgart and MPI for Solid University State Research), completing his PhD thesis in 2013. Being awarded a Feodor Lynen postdoctorial scholarship (Alexander von Humboldt Foundation), he joined the group of A. Paul Alivisatos at UC Berkeley. Since 2015, he has been

a head of nanofabrication at the Fourth Physics Institute at University of Stuttgart.

Chao Meng received his BS and PhD degrees in optical engineering from Zhejiang University, Hangzhou, China, in 2008 and 2013, respectively. During 2014 to 2017, he was a team leader of Shanghai Silight Technology for commercializing silicon photonics. He is currently a postdoctoral fellow at the Centre for Nano Optics, University of Southern Denmark, Odense, Denmark. His current research interests include nanophotonics, plasmonics, and metasurfaces. He was a recipient of the Marie S.-Curie MULTIPLY fellowship in 2019.

Sören im Sande received his bachelor's degree from TU Lübeck and his master's degree from the University of Southern Denmark. He is currently a PhD research fellow at the Centre for Nano Optics of the University of Southern Denmark. His work is focused on plasmonic metasurfaces, integrated photon sources, as well as quantum metasurfaces.

Harald Giessen is a full professor and holds the chair for ultrafast nano-optics in the Department of Physics at the University of Stuttgart. He is also co-chair of Stuttgart Center of Photonics Engineering. He is a fellow of the Optical Society of America. His research interests include ultrafast nano-optics, plasmonics, metamaterials, 3D-printed micro- and nano-optics, medical micro-optics, miniature endoscopy, innovative MID-IR ultrafast laser sources, applications in microscopy, biology, and sensing.

Fei Ding received his PhD in optical engineering from Zhejiang University in 2015. He is currently an assistant professor at the University of Southern Denmark. His current research interests include metasurfaces, plasmonics, and quantum nanophotonics. He has published more than 65 articles in peer-reviewed journals. He won the Wang Daheng Optical prize, the Young Scientist Award from the Progress in Electromagnetics Research Symposium, Villum Young Investigator, and the DOPS award.

Sergey I. Bozhevolnyi is a professor and head of the Centre for Nano Optics at the University of Southern Denmark and Chair of Technical Science at the Danish Institute of Advanced Study. His current research interests include linear and nonlinear nano-optics and plasmonics, including plasmonic interconnects, quantum plasmonics and metasurfaces. He is a fellow of Optical Society of America (2007), an elected member of Danish Academies of Natural Sciences (2010) and Technical Sciences (2019).